

Keyhole Imaging: Non-Line-of-Sight Imaging and Tracking of Moving Objects Along a Single Optical Path at Long Standoff Distances

Christopher A. Metzler
Stanford University
cmetzler@stanford.edu

David B. Lindell
Stanford University
lindell@stanford.edu

Gordon Wetzstein
Stanford University
gordon.wetzstein@stanford.edu

Abstract

Non-line-of-sight (NLOS) imaging and tracking is an emerging paradigm that allows the shape or position of objects around corners or behind diffusers to be recovered from transient measurements. However, existing NLOS approaches require the imaging system to scan a large area on a visible surface, where the indirect light paths of hidden objects are sampled. In many applications, such as robotic vision or autonomous driving, optical access to a large scanning area may not be available, which severely limits the practicality of existing NLOS techniques. Here, we propose a new approach, dubbed keyhole imaging, that captures a sequence of transient measurements along a single optical path at long standoff distances, for example through a keyhole. Assuming that the hidden object of interest moves during the acquisition time, we capture a series of time-resolved projections of the object’s shape from unknown viewpoints. We derive inverse methods based on Expectation-Maximization to recover the object’s shape and location using these measurements, and we demonstrate successful experimental results with a prototype keyhole imaging system.

1 Introduction

Imaging or tracking objects outside a camera’s direct line of sight has important applications in autonomous driving, robotic vision, and many other areas. By analyzing the time of flight of indirectly scattered light, transient non-line-of-sight (NLOS) imaging approaches (e.g., [45, 9, 15, 29, 51, 28, 26]) are a particularly promis-

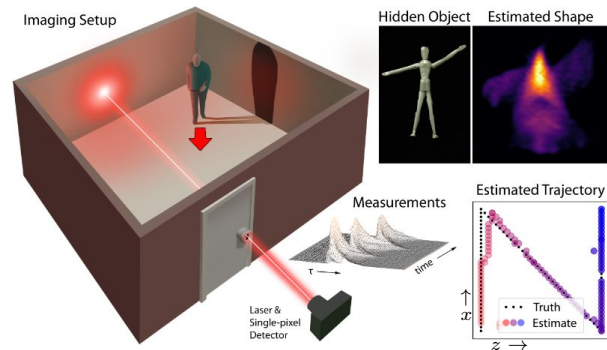


Figure 1: **Keyhole imaging.** A time-resolved detector and pulsed laser illuminate and image a point visible through a keyhole (left). As a hidden person moves, the detector captures a series of time-resolved measurements of the light which scatters to the person and back (center). From these measurements, we reconstruct both hidden object shape (e.g., for a hidden mannequin) and the time-resolved trajectory (right).

ing approach to seeing around corners at large scales and long standoff distances. However, all of these techniques rely on time-resolved measurements of indirect light transport that are captured by sampling a large area of a surface within the line of sight of the imaging system. The sampled area acts as a synthetic aperture and it was shown that the resolution of estimated hidden scenes, and also the accuracy of NLOS tracking, is primarily limited by both size of the sampling area and temporal resolution of the imaging system [29]. Unfortunately, in many applications, such as navigation in tight quarters or at long stand-offs, optical access to a large sampling surface may

not be feasible, making current NLOS techniques impractical.

Here, we introduce a new paradigm for NLOS imaging where transient measurements are recorded along a single optical path at a long standoff distance. As shown in Figure 1, one example of an optical configuration that is enabled by our approach is that of imaging a single point on the wall of a room through a keyhole. Although imaging through a keyhole may be possible by moving a small camera very close to the keyhole, our approach operates at long standoff distances and only requires a single optical path from the light source–detector pair to the sampling point inside the room.

Trying to recover the 3D shape or to track the location of objects in a static room with such a configuration is a highly ill-posed problem. However, as was recognized by Bouman et al. [8], object motion can make otherwise ill-posed NLOS imaging problems tractable. Unlike their work, however, keyhole imaging only has access to a single optical light path. To account for this, our work makes use of the intuition that *measurements of a moving object captured with a fixed sensor are equivalent to measurements of a fixed object captured with a moving “virtual” sensor*. This is the same principle that underlies problems in other domains, such as inverse synthetic aperture radar (ISAR) [33]. Just as NLOS imaging is analogous to SAR and tomography [27], keyhole imaging of a moving object is analogous to ISAR and unknown-view tomography. Like ISAR and unknown-view tomography, keyhole imaging requires solving a challenging and highly non-convex inverse problem: jointly estimating both the shape of the hidden object and its unknown motion. We address this problem using a variant of the Expectation-Maximization (EM) algorithm.

To our knowledge, this is the first work to study the keyhole imaging problem, which could enable an entirely new class of NLOS imaging problems to be addressed. In doing so, this work makes several distinct contributions:

- We introduce the keyhole imaging problem: NLOS imaging or tracking where the relay wall consists of just a single visible point.
- We develop a Bayesian algorithm based on Expectation-Maximization (EM) that uses the unknown motion of the object to solve the keyhole imaging problem.

- We evaluate the performance of this method for various types of motions in extensive simulations.
- We build a prototype system and experimentally demonstrate NLOS imaging and tracking through a keyhole.

2 Related Work

NLOS Imaging and Tracking While long theorized [14, 23], NLOS imaging of static objects was first successfully demonstrated in 2012 [46]. Since then, much progress has been made on developing more efficient data acquisition setups and inverse methods. The majority of these works reconstruct hidden scenes from transient measurements captured using pulsed [31, 45, 50, 16, 43, 1, 32, 29, 52, 9, 29, 17, 51, 28, 26] or continuous-wave [18, 19] active illumination, or using a coherent source that creates speckle [6, 21, 20, 47, 51]. Acoustic NLOS imaging has also been explored [25], as have methods that forgo active illumination and instead rely opportunistically on illumination sources in the scene itself or occlusions [42, 8, 5, 41, 34]. All these works require a large relay wall to sample the indirect light transport inside their line of sight.

More recently, several groups have developed methods to image or track moving hidden objects. This feat can be accomplished by either ignoring motion and using powerful illumination to form frame-by-frame reconstructions in real-time [30, 26] or by leveraging the differences between subsequent frames with object motion to track them [24, 15, 10, 8, 39, 7]. These methods too rely upon a large relay wall.

Keyhole imaging is a new NLOS imaging modality. Unlike other NLOS approaches, it only requires access to a single optical light path and it operates at long standoff distances. The inverse keyhole imaging problem is significantly more challenging than conventional NLOS imaging because (i) the location of the sampling points is unknown and (ii) object motion is typically constrained to 1D trajectories, severely restricting measurement diversity.

Unknown-view Tomography is the problem of reconstructing a 3D or 2D object from a series of 2D or 1D pro-

jections, respectively, taken at unknown view angles [4]. This problem occurs in a number of applications; most notably inverse synthetic aperture radar (ISAR) [33] and single-particle cryogenic electron microscopy [11, 37].

A host of methods exist to solve the unknown-view tomography problem: moment methods compute perspective invariant features and use these features to directly reconstruct the scene [48, 2, 53]. Low-dimensional embedding methods estimate the perspective associated with each measurement by embedding it into a low-dimensional space, this estimated perspective then allows for the application of standard recovery algorithms [12, 38]. Bayesian methods, which are the most popular and successful approach to unknown-view tomography, compute maximum likelihood (ML) or maximum a posteriori (MAP) estimates of the scene under priors on the distribution of the scene, the measurements, and the noise [3, 35]. Bayesian methods are sample efficient and highly robust to noise, but can be computationally demanding.

Keyhole imaging is a particularly challenging unknown view tomography problem as it reconstructs an image of a 3D object from unregistered 1D measurements. Nevertheless, we found Bayesian algorithms could be adapted to solve this problem. To overcome their high computational cost we took advantage of GPU computing.

3 Keyhole Imaging

The keyhole imaging setup is illustrated in Figure 1. A confocal pulsed light source–detector pair, placed at a large standoff distance, illuminates and images a visible point through a small aperture (such as a keyhole). The time-resolved measurements, captured with a single-photon avalanche diode (SPAD) or other detector, contain the temporal response of the emitted light pulse that travels to a visible point through the keyhole, and scatters back from a hidden object. A series of measurements, captured as the hidden object undergoes rigid motion, are used to recover the shape and motion of the hidden object.

In this section, we describe the keyhole measurement model in detail and derive a Bayesian estimation method for recovering the shape and motion of hidden objects.

3.1 Observation Model

Assume that the hidden object is defined by a volumetric albedo $\rho(\mathbf{x}')$, where $\mathbf{x}' = [x', y', z']^T$ is the object’s local coordinate system. A rigid transform $\theta_i = [\mathbf{R}_i | \mathbf{t}_i] \in \mathbb{R}^{3 \times 4}$ describes the motion of the object at some time i and transforms it into the global coordinate system, using rotation and translation, as $\mathbf{x} = \mathbf{R}_i \mathbf{x}' + \mathbf{t}_i$. Each time-resolved measurement $\mathbf{y}_i \in \mathbb{R}^T$, represented by a histogram with T bins counting the number of photon-arrival events within a certain time window, is defined by a formation model

$$\mathbf{y}_i = f(\rho, \theta_i) + \boldsymbol{\eta}_i, \quad (1)$$

where $\boldsymbol{\eta}_i$ denotes noise and $f(\rho, \theta_i)$ is the NLOS imaging forward model

$$f(\rho, \theta_i) = \int \frac{1}{g(\mathbf{x})} \rho(\mathbf{x}') \delta(2\|\mathbf{x}\|_2 - \tau c) d\mathbf{x}'. \quad (2)$$

Here, c is the speed of light, τ is the time relative to an emitted laser pulse, the point at which we record the scene is located in the origin of the global coordinate system, and $g(\mathbf{x})$ describes the falloff of light with distance. For example, hidden objects with Lambertian reflectance exhibit a falloff of $g_{\text{diffuse}}(\mathbf{x}) = \|\mathbf{x}\|_2^4$ whereas perfectly retroreflective objects experience $g_{\text{retro}}(\mathbf{x}) = \|\mathbf{x}\|_2^2$ [29]. Moreover, g can also include angle-dependent factors that are influenced by the surface normals, the normal of the visible wall, or other angle-dependent reflectance characteristics. Using experimental measurements, we found that $g_{\text{exp}}(\mathbf{x}) = \|\mathbf{x}\|_2^4 \cos^4(\phi)$ best modeled a patch of retroreflective material used in our captured results and oriented parallel to the visible wall, where ϕ is the angle between the wall’s normal and \mathbf{x} .

Note that Equation (2) is the standard confocal NLOS model [29], with the hidden object’s position transformed by θ_i . The keyhole imaging reconstruction problem uses a series of measurements $\mathbf{y}_1, \dots, \mathbf{y}_L$ to reconstruct the albedo ρ in its local coordinate system. This problem is challenging because the measurements are parameterized by latent hidden object locations, $\theta_1, \dots, \theta_L$ corresponding to each captured measurement.

3.2 Reconstruction with Expectation-Maximization

We seek to recover an estimate of the unknown albedo, ρ from the observations $\mathbf{y}_1, \dots, \mathbf{y}_L$. This can be done by maximizing the log likelihood of the observed measurements

$$\mathcal{L}(\rho; \mathbf{y}) = \log p(\mathbf{y}|\rho) = \log \int_{\boldsymbol{\theta}} p(\mathbf{y}, \boldsymbol{\theta}|\rho) d\boldsymbol{\theta}, \quad (3)$$

where $\mathbf{y} = [\mathbf{y}_1, \dots, \mathbf{y}_L]$ and $\boldsymbol{\theta} = [\boldsymbol{\theta}_1, \dots, \boldsymbol{\theta}_L]$.

Maximizing the objective (3) directly is numerically unstable. Instead, in this work we utilize EM, which efficiently maximizes (3) by solving a series of easy-to-solve least squares problems. In particular, EM iteratively applies two steps: (1) an expectation step in which an estimated conditional distribution of $\boldsymbol{\theta}$ is used to form a lower bound to the log likelihood, and (2) a maximization step, which estimates the albedo given the current conditional distribution of $\boldsymbol{\theta}$.

EM Algorithm for Keyhole Imaging

Given an estimate $\rho^{(n)}$ of the hidden object's albedo at iteration n of the EM algorithm, we perform the expectation step by finding a lower bound on the log of the likelihood given by Equation (3). Using Jensen's inequality, it can be shown that a lower bound is given as $Q(\rho, \rho^{(n)})$ [13], such that, up to additive constants,

$$\begin{aligned} Q(\rho, \rho^{(n)}) &= \mathbb{E}_{\boldsymbol{\theta}|\mathbf{y}, \rho^{(n)}}[\log p(\mathbf{y}, \boldsymbol{\theta}|\rho)], \\ &= \int_{\boldsymbol{\theta}} p(\boldsymbol{\theta}|\mathbf{y}, \rho^{(n)}) \log[p(\mathbf{y}|\boldsymbol{\theta}, \rho)p(\boldsymbol{\theta}|\rho)] d\boldsymbol{\theta}, \\ &= \sum_{i=1}^L \int_{\boldsymbol{\theta}} p(\boldsymbol{\theta}|\mathbf{y}_i, \rho^{(n)}) \log[p(\mathbf{y}_i|\boldsymbol{\theta}, \rho)p(\boldsymbol{\theta}|\rho)] d\boldsymbol{\theta}, \\ &\approx \sum_{i=1}^L \sum_{\boldsymbol{\theta}_k \in \Omega} p(\boldsymbol{\theta}_k|\mathbf{y}_i, \rho^{(n)}) \log[p(\mathbf{y}_i|\boldsymbol{\theta}_k, \rho)p(\boldsymbol{\theta}_k|\rho)], \\ &= \sum_{i=1}^L \sum_{\boldsymbol{\theta}_k \in \Omega} p(\boldsymbol{\theta}_k|\mathbf{y}_i, \rho^{(n)}) \log[p(\mathbf{y}_i|\boldsymbol{\theta}_k, \rho)]. \end{aligned} \quad (4)$$

Here, Ω is the domain of possible hidden object positions (parameterized as rigid transforms); $p(\boldsymbol{\theta}_k|\mathbf{y}_i, \rho^{(n)})$ is the probability the object is at position $\boldsymbol{\theta}_k$ during the i^{th} measurement conditioned on the measurement \mathbf{y}_i and the previous estimate of the object's albedo $\rho^{(n)}$; and $p(\mathbf{y}_i|\boldsymbol{\theta}_k, \rho)$

is the likelihood the measurement \mathbf{y}_i would be observed, conditioned on the object being at position $\boldsymbol{\theta}_k$ and the current estimate of the albedo $\rho^{(n)}$.

In the above expression, the second line depends on Bayes' rule; the third line holds by assuming the observations are independent; the fourth line uses a discrete approximation of the hidden object location, which is required for our numerical implementation; and the last line's equality holds by assuming that the object's location is independent of its albedo.

In the case of additive white Gaussian noise with variance σ^2 , Equation (4) simplifies to

$$Q(\rho, \rho^{(n)}) \propto \sum_{i=1}^L \sum_{\boldsymbol{\theta}_k \in \Omega} w_{i, \boldsymbol{\theta}_k} \left(-\|\mathbf{y}_i - f(\rho, \boldsymbol{\theta}_k)\|_2^2 \right), \quad (5)$$

where $w_{i, \boldsymbol{\theta}_k} = \exp \frac{-\|\mathbf{y}_i - f(\rho^{(n)}, \boldsymbol{\theta}_k)\|_2^2}{2\sigma^2}$. (While EM allows more accurate noise models [36] to be used, an i.i.d. Gaussian model reduces the computational complexity of the algorithm.) Intuitively, this result computes the sum of squared differences between the measurements and predicted measurements given the current estimate of ρ and each possible hidden object location. Elements of the sum are weighted by $w_{i, \boldsymbol{\theta}_k}$, which is proportional to the conditional probability that the hidden object is at location $\boldsymbol{\theta}_k$ for measurement \mathbf{y}_i .

Then, the maximization step of the algorithm computes

$$\rho^{(n+1)} = \arg \max_{\rho} Q(\rho, \rho^{(n)}). \quad (6)$$

for $n = 1 \dots N$. This optimization can be accomplished using gradient descent until convergence.

We summarize the EM algorithm for keyhole imaging in Algorithm 1. At a high level, the two steps of EM for keyhole imaging can be understood as follows. First, based on the current estimate of ρ , line 3 of the algorithm performs the expectation step and estimates the probability of measurement \mathbf{y}_i being captured at each of the possible hidden object locations $\boldsymbol{\theta}_k$. This can also be interpreted as performing a soft assignment of the object position at each iteration. Next, line 4 computes the maximization step. Based on the soft assignment of hidden object location, the algorithm updates the estimate of the hidden object albedo. Iterating these two steps until convergence produces the final estimate of the hidden object

Algorithm 1 EM for Keyhole Imaging

- 1: Initialize: $\rho^{(0)}$
 - 2: **for** $n=0, 1, \dots, N-1$ **do**
 - 3: Compute $w_{i,\theta_k} = \exp \frac{-\|\mathbf{y}_i - f(\rho^{(n)}, \theta_k)\|_2^2}{2\sigma^2} \forall i, k$
 - 4: $\rho^{(n+1)} = \arg \max_{\rho} Q(\rho, \rho^{(n)})$
 - 5: **Return** $\rho^{(N)}$
-

albedo, while also recovering an estimate of the distribution of the hidden object’s locations during each measurement.

Adding Priors EM can be extended to computing MAP estimates by redefining $Q(\rho, \rho^{(n)})$ as

$$\sum_{i=1}^L \sum_{\theta_k \in \Omega} w_{i,\theta_k} \left(-\|\mathbf{y}_i - f(\rho, \theta_k)\|_2^2 + \lambda \log p(\rho) \right), \quad (7)$$

where $p(\rho)$ is a prior on ρ . In this work, we use $\log p(\rho) = -\|\mathbf{L}\rho\|_1 - \|\rho\|_1$, where \mathbf{L} is a Laplacian filter. This expression corresponds to a prior that the hidden object’s albedo is smooth and sparse.

Implementation Details We developed a Pytorch implementation of EM which we ran for 30 iterations. Each maximization step was accomplished by running the ADAM optimizer [22] $n + 1$ times, where n is the EM iteration number. During the early iterations of the algorithm, when our estimate of w is unreliable, we do not spend much time optimizing ρ . We set ADAM’s learning rate to 0.1 and set its β values, which control the momentums’ decay, to 0.5 and 0.999. We set the regularization parameter λ to 2000. The noise variance σ was set to 200 for both simulated and experimental data; this value is far larger than the true noise variance, but helped account for model mismatch and the discretization of the trajectory support set Ω .

During simulations, Ω was a 1 meter by 1 meter 33×33 equispaced grid. For experiments, Ω was a 33×33 grid spanning 1 m along the axis parallel to the wall and 15 cm along the axis perpendicular to the wall; this was the range of our translation stages. We enforced positivity on ρ by parameterizing it with the variable ν , with $\rho := \nu^2$

where the square is taken elementwise. The variable ν was initialized with an i.i.d. Gaussian vector.

We found that deterministic annealing helped EM avoid local minima [44]. With deterministic annealing

$$w_{i,\theta_k} = \left[\exp \frac{-\|\mathbf{y}_i - f(\rho^{(n)}, \theta_k)\|_2^2}{2\sigma^2} \right]^\beta, \quad (8)$$

where $\beta \in (0, 1]$ is a temperature parameter that increases iteration to iteration. We set $\beta^{(n+1)} = 1.3 \cdot \beta^{(n)}$, with $\beta^{(0)}$ set such that $\beta^{(N-1)} = 1$. Annealing serves to make the distribution of the estimated object locations more uniform during the earlier iterations of the algorithm, when the algorithm has a less accurate estimate of ρ .

Code and data will be made available.

4 Evaluation and Analysis

4.1 Simulation Setup

We first investigate the keyhole imaging problem in simulation. The keyhole measurements are simulated from nine different binary objects, drawn from the HaSyV2 dataset [40], which are illustrated in the top row of Figure 3. Each of these objects has a resolution of 64×64 and is 50 cm tall and wide in the simulator. Our simulated SPAD measurements have a temporal resolution of 16 ps. We apply Poisson noise to the measurements such that they have the desired SNR for each test.

For each of the nine objects, we simulate measurements from nine distinct trajectories of varying lengths. The virtual sensor locations corresponding to each of these trajectories is shown in Figure 2. Recall measurements of a moving object with a fixed sensor location are equivalent to measurements of a fixed object with a moving virtual sensor. Three of these trajectories (left column) have the virtual sensor locations restricted to a constant z plane; this corresponds to object roll and translation up-and-down and side-to-side. Another three of these trajectories (middle column) have the virtual sensor locations restricted to a constant x plane; this corresponds to object pitch and translation up-and-down and forward-and-backward. The last three of these trajectories (right column) have the virtual sensor locations restricted to a constant y plane; this corresponds to object yaw and translation side-to-side and forward-and-backward. The hori-

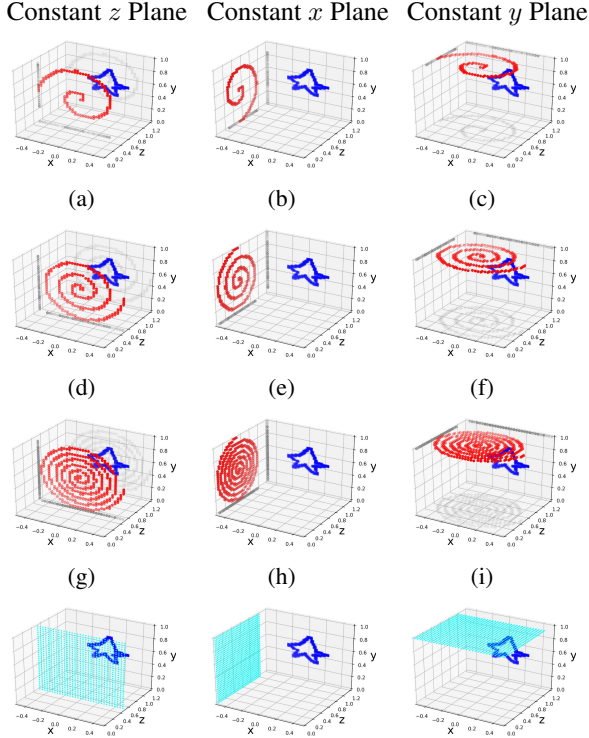


Figure 2: **Simulation setup.** We simulated reconstructing objects which followed the nine sampling trajectories (a-i) shown in the top three rows. Each plot displays an example object in blue and the locations of the virtual sensor locations in red. The plots in the bottom row show the allowable virtual sensor locations used by EM when reconstructing any of the three trajectories displayed above them.

horizontal motion in the last of these trajectories is arguably the most realistic; for instance, this is the type of motion exhibited by a car. The last row of Figure 2 presents the 33×33 grids Ω of allowable virtual sensor locations that we use with EM.

Because the EM algorithm does not know the object trajectories beforehand, the algorithm’s reconstructions have certain ambiguities/invariances. Constant z trajectories are rotation invariant: Given a reconstructed trajectory and an object that fits the measurements, one could rotate both clockwise without changing the fit. Similarly, constant x trajectories are invariant to vertical flips of the trajectory and object and constant y trajectories are invari-

ant to horizontal flips.

When considered as object/trajectory pairs, none of the reconstructions are invariant to translations. However, an object/trajectory pair can be expressed as an equivalent pair where the object is translated one direction and the trajectory is translated equally in the opposite direction. Thus, in comparing our reconstructed objects to the ground truth, we need to compare across translations as well.

4.2 Simulation Results

In order to form a performance baseline, we first reconstruct the hidden objects assuming their trajectories are known. This is accomplished by maximizing the log-likelihood

$$\sum_{i=1}^L -\|\mathbf{y}_i - f(\rho, \boldsymbol{\theta}_i)\|_2^2 + \lambda \log p(\rho), \quad (9)$$

where the objects’ locations over time, $\boldsymbol{\theta}_1, \dots, \boldsymbol{\theta}_L$, are given. We use 200 iterations of gradient descent (GD), along-side the ADAM optimizer, to maximize (9).

We compare EM and GD qualitatively in Figure 3 and quantitatively in Table 1. Table 1 reports reconstruction accuracy in terms of disambiguated Structural Similarity (SSIM) [49], which we define as

$$\max_{\text{rtf} \in \text{RTF}} \text{SSIM}(\rho, \text{rtf}(\hat{\rho})), \quad (10)$$

where $\hat{\rho}$ denotes the reconstructed albedo and RTF denotes the set of all possible rotations, translations, and flips of the object. We test over all rotations in 5° increments and all translations in 1 pixel increments.

Figure 3 compares reconstructions between GD and EM when the object follows trajectory (f) from Figure 2 and the measurements have an SNR of 15. The results show EM performs nearly as well as GD. However, the reconstructions of some of the simpler objects (for which the correspondence between virtual sensor location and measurement is more ambiguous) do have artifacts. Table 1 demonstrates EM performs only a little worse than GD across a variety of SNRs and trajectories. This general trend holds as we move to real-world data as well.

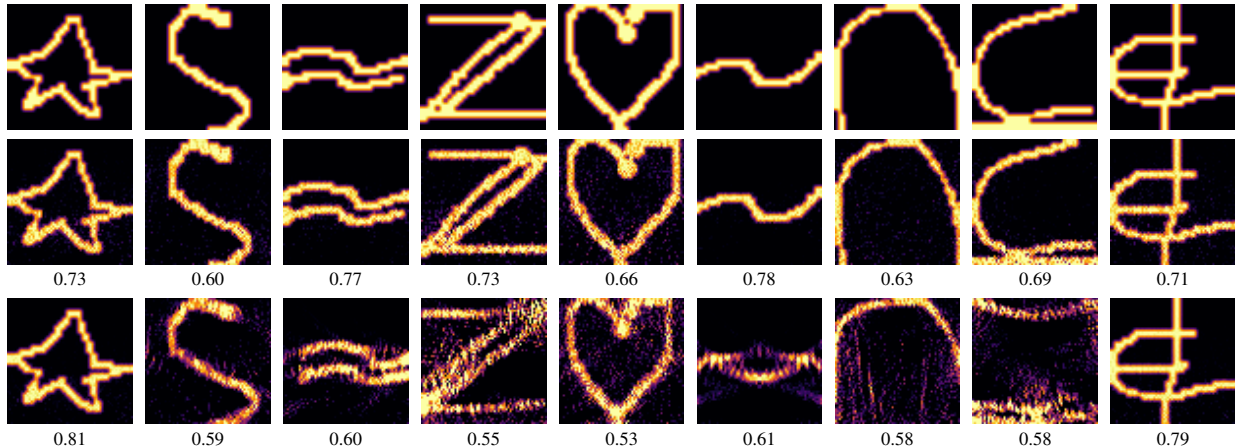


Figure 3: **Simulation results.** Top: The nine test objects. Middle: Known-trajectory reconstructions using gradient descent with simulated measurements that follow trajectory (f) from Figure 2 and have an SNR of 15. Bottom: Unknown-trajectory reconstructions using EM with the same simulated measurements. Below each reconstruction we report the disambiguated SSIM.

	SNR = 5		SNR = 15		SNR = 50	
	GD	EM	GD	EM	GD	EM
Trajectory (a)	0.56	0.55	0.66	0.57	0.75	0.58
Trajectory (b)	0.55	0.49	0.64	0.50	0.72	0.51
Trajectory (c)	0.59	0.57	0.69	0.57	0.77	0.59
Trajectory (d)	0.59	0.55	0.68	0.58	0.77	0.57
Trajectory (e)	0.58	0.48	0.66	0.48	0.73	0.50
Trajectory (f)	0.62	0.60	0.70	0.63	0.79	0.64
Trajectory (g)	0.61	0.58	0.70	0.58	0.80	0.59
Trajectory (h)	0.60	0.51	0.68	0.52	0.76	0.53
Trajectory (i)	0.65	0.61	0.72	0.63	0.81	0.65

Table 1: Comparison of the mean disambiguated SSIM (higher is better) across the 9 tests images with various trajectories and SNRs. EM works best with long trajectories, but is relatively robust to noise.

5 Experimental Validation

5.1 Experimental Setup

Our prototype system is illustrated in Figure 4. The optical setup consists of a 670 nm pulsed laser source (ALPHALAS PICOPOWER-LD-670-50) operating with a 10 MHz repetition rate, an average power of approxi-

mately 0.1 mW, and a pulse width of 30 ps. This laser is in a confocal configuration with a fast-gated single-pixel SPAD detector (Micro Photon Devices PDM series SPAD, $50 \mu\text{m} \times 50 \mu\text{m}$ active area), which allows us to gate out direct bounce photons, capturing only indirect photons from the hidden object. A time-correlated single photon counter (PicoQuant PicoHarp 300) takes as input a trigger signal from the laser and photon detection event triggers from the SPAD and forms time-stamped histograms of photon arrival times with 16 ps bin widths.

We captured keyhole measurements of the objects illustrated in the top row of Figure 5. The objects are each 50 cm tall and covered in retroreflective tape. The objects were affixed to two Zaber translation stages: a 1 m linear stage (X-BLQ1045-E01) and a 15 cm stage (T-LSR150A). Using the stages, objects can be translated to any point within a 1 m by 15 cm horizontal plane, where the long axis (x -axis) is aligned parallel to the wall and the short axis (z -axis) is aligned perpendicular to the wall. In the captured measurements, objects are translated to between 66 and 165 discrete locations. To capture adequate signal given the limited laser power of our prototype, the objects hold position at each location for 10 seconds. Example trajectories are shown in the last column of Figure 5.

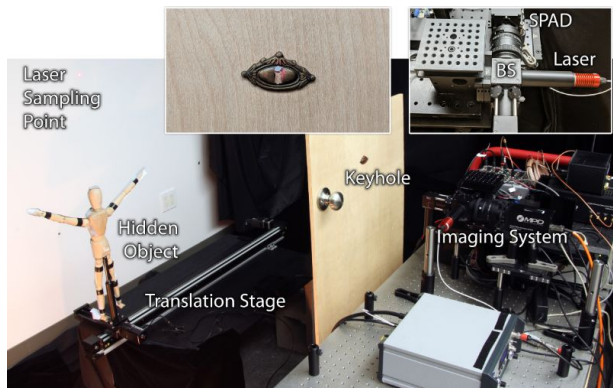


Figure 4: **Experimental setup.** Our optical system sends a laser pulse through the keyhole of a door. On the other side of the door, the hidden object moves along a translation stage. When third-bounce photons return, they are recorded and time-stamped by a SPAD. Top-right inset: A beam splitter (BS) is used to place the laser and SPAD in a confocal configuration.

5.2 Experimental Results

As in the previous section, in order to form a performance baseline, we first reconstruct the hidden objects using GD assuming their trajectories were known. The resulting reconstructions are presented in the second row of Figure 5. The reconstructions illustrate that (x, z) translations contain the measurement diversity necessary to perform NLOS reconstructions with real data. The mannequin’s pose is recognizable and the letters are all readable.

For the case where object trajectories are not known, we use EM to recover both the shape and trajectory of the hidden object. For each measurement, EM also produces an estimate of the probability distribution of each object’s location. We select the highest probability location as the location estimate.

The reconstructed objects and trajectories are presented in the third and fourth rows of Figure 5. Again the mannequin’s pose is recognizable and the letters are all readable. Moreover, EM’s estimated trajectories closely match the ground truth and in all four examples the general path of the object is clearly visible.

The EM reconstruction of the ‘K’ serves to illustrate the translation ambiguity that was discussed in Section 4.1. Relative to the true trajectory, the reconstructed tra-

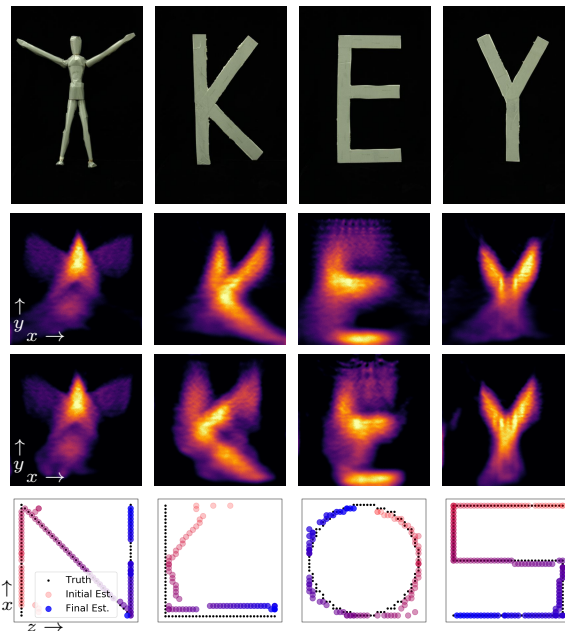


Figure 5: **Experimental results.** First row: Images of the hidden objects. Second row: Reconstructions of the hidden objects using GD when their trajectories are known. Third row: EM reconstructions of the hidden objects when their trajectories are unknown. Fourth row: EM estimates of the trajectories of the hidden objects, where dot color indicates position over time.

jectory is displaced by a positive shift in the x direction. Meanwhile, the object reconstruction is offset by a negative shift in the x direction. Considered jointly, the object’s location is recovered accurately.

The EM reconstructions were computed at 256×256 resolution in five and a half minutes using a Titan RTX GPU and a six core Intel CPU. The known-trajectory GD reconstructions took fifteen seconds on the same hardware.

6 Discussion

This work proposes, develops, and experimentally validates keyhole imaging—a new technique to reconstruct the shape and location of a hidden object from NLOS measurement captured along a single optical path. The proposed recovery method relies on object motion to

gather the measurement diversity needed for reconstruction. Our experiments demonstrate that horizontal object motion provides enough measurement diversity to produce excellent tracks of an object’s location and reasonable reconstructions of an object’s albedo.

Limitations While our reconstructions contain artifacts, these can be attributed to the challenging sampling geometry associated with keyhole imaging of an object moving along a horizontal plane. For vertically-oriented objects (i.e. along x and y), horizontal object motion (along x and z) corresponds to a sampling pattern with low measurement diversity along the reconstructed image plane. This is fundamentally more challenging than the standard NLOS configuration, where the measurement diversity along x and y is aligned with the image plane. Thus even when object location is known, as in the GD results, some artifacts result.

Because of the limited power of our laser, our experiments did not reconstruct a continuously moving object. Rather, our object rested 10 seconds at a series of points on a known 33×33 grid. However, imaging objects with continuous motion could potentially be achieved using a more powerful laser, such as those used in other non-line-of-sight imaging work [28, 26], which are $10\,000\times$ brighter than ours. Resolving finer object trajectories could also be achieved by increasing the resolution of the reconstruction grid, though at increased computational cost.

Future Work Several avenues exist to improve the proposed EM-based reconstruction scheme. First, the present algorithm ignores the fact that motion is generally continuous; that is it treats a motion trajectory that bounces back and forth across the room just as likely as a smooth straight path. To address this, motion-continuity and other priors on θ could be incorporated and fit naturally into the EM framework. Second, while our current method imposes smoothness and sparsity on the reconstruction, more advanced priors, particularly learned priors, could greatly aid in the reconstruction. Third, our present results restrict the trajectories to one of three planes. While our implementation supports three dimensional trajectories, they also require significantly more computation. De-

veloping more efficient algorithms and implementations could make our method more generalizable. Finally, extending our algorithm to handle non-rigid body motion is an important open problem.

7 Conclusion

NLOS imaging has emerged as an important research direction in the computer vision community and is widely recognized for enabling capabilities that would have been impossible only a few years ago. While seeing around corners has long required imaging a large visible surface, we demonstrate imaging and tracking using a single visible point by exploiting object motion. Moreover, combining time-of-flight imaging with object motion may be useful for other 3D imaging applications. We envision that keyhole imaging could unlock new applications, such as NLOS imaging in constrained and cluttered environments.

References

- [1] Victor Arellano, Diego Gutierrez, and Adrian Jarabo. Fast back-projection for non-line of sight reconstruction. *Opt. Express*, 25(10):11574–11583, 2017.
- [2] Afonso S. Bandeira, Philippe Rigollet, and Jonathan Weed. Optimal rates of estimation for multi-reference alignment. *arXiv preprint arXiv:1702.08546*, 2017.
- [3] Samit Basu and Yoram Bresler. Feasibility of tomography with unknown view angles. *IEEE Trans. Image Process.*, 9(6):1107–1122, 2000.
- [4] Samit Basu and Yoram Bresler. Uniqueness of tomography with unknown view angles. *IEEE Trans. Image Process.*, 9(6):1094–1106, 2000.
- [5] Mufeed Batarseh, S. Sukhov, Zhiqin Shen, Heath Gemar, Reza Rezvani, and Aristide Dogariu. Passive sensing around the corner using spatial coherence. *Nature Communications*, 9(1):3629, 2018.
- [6] Jacopo Bertolotti, Elbert G. van Putten, Christian Blum, Ad Lagendijk, Willem L. Vos, and Allard P. Mosk. Non-invasive imaging through opaque scattering layers. *Nature*, 491(7423):232, 2012.
- [7] Jeremy Boger-Lombard and Ori Katz. Passive optical time-of-flight for non line-of-sight localization. *Nature Communications*, 10, 2019.

- [8] Katherine L. Bouman, Vickie Ye, Adam B. Yedidia, Frédo Durand, Gregory W. Wornell, Antonio Torralba, and William T. Freeman. Turning corners into cameras: Principles and methods. In *Proc. ICCV*, 2017.
- [9] Mauro Buttafava, Jessica Zeman, Alberto Tosi, Kevin Elieceiri, and Andreas Velten. Non-line-of-sight imaging using a time-gated single photon avalanche diode. *Opt. Express*, 23(16):20997–21011, 2015.
- [10] Susan Chan, Ryan E. Warburton, Genevieve Gariepy, Jonathan Leach, and Daniele Faccio. Non-line-of-sight tracking of people at long range. *Opt. Express*, 25(9):10109–10117, 2017.
- [11] Yifan Cheng, Nikolaus Grigorieff, Pawel A. Penczek, and Thomas Walz. A primer to single-particle cryo-electron microscopy. *Cell*, 161(3):438–449, 2015.
- [12] Ronald R Coifman, Yoel Shkolnisky, Fred J. Sigworth, and Amit Singer. Graph laplacian tomography from unknown random projections. *IEEE Trans. Image Process.*, 17(10):1891–1899, 2008.
- [13] Frank Dellaert. The expectation maximization algorithm. Technical report, Georgia Institute of Technology, 2002.
- [14] Isaac Freund. Looking through walls and around corners. *Physica A: Statistical Mechanics and its Applications*, 168(1):49–65, 1990.
- [15] Genevieve Gariepy, Francesco Tonolini, Robert Henderson, Jonathan Leach, and Daniele Faccio. Detection and tracking of moving objects hidden from view. *Nature Photonics*, 10:23–26, 2016.
- [16] Otkrist Gupta, Thomas Willwacher, Andreas Velten, Ashok Veeraraghavan, and Ramesh Raskar. Reconstruction of hidden 3d shapes using diffuse reflections. *Opt. Express*, 20(17):19096–19108, Aug 2012.
- [17] Felix Heide, Matthew O’Toole, Kai Zang, David B. Lindell, Steven Diamond, and Gordon Wetzstein. Non-line-of-sight imaging with partial occluders and surface normals. *ACM Trans. Graph.*, 38(3):22, 2019.
- [18] Felix Heide, Lei Xiao, Wolfgang Heidrich, and Matthias B. Hullin. Diffuse mirrors: 3d reconstruction from diffuse indirect illumination using inexpensive time-of-flight sensors. In *Proc. CVPR*, 2014.
- [19] Achuta Kadambi, Hang Zhao, Boxin Shi, and Ramesh Raskar. Occluded imaging with time-of-flight sensors. *ACM Trans. Graph.*, 35(2):15, 2016.
- [20] Ori Katz, Pierre Heidmann, Mathias Fink, and Sylvain Gigan. Non-invasive single-shot imaging through scattering layers and around corners via speckle correlations. *Nature Photonics*, 8(10):784, 2014.
- [21] Ori Katz, Eran Small, and Yaron Silberberg. Looking around corners and through thin turbid layers in real time with scattered incoherent light. *Nature Photonics*, 6(8):549–553, 2012.
- [22] Diederik P. Kingma and Jimmy Ba. Adam: A method for stochastic optimization. *arXiv preprint arXiv:1412.6980*, 2014.
- [23] A. Kirmani, T. Hutchison, J. Davis, and R. Raskar. Looking around the corner using transient imaging. In *Proc. ICCV*, 2009.
- [24] Jonathan Klein, Christoph Peters, Jaime Martín, Martin Laurenzis, and Matthias B. Hullin. Tracking objects outside the line of sight using 2d intensity images. *Scientific Reports*, 6:32491, 2016.
- [25] David B. Lindell, Gordon Wetzstein, and Vladlen Koltun. Acoustic non-line-of-sight imaging. In *Proc. CVPR*, 2019.
- [26] David B. Lindell, Gordon Wetzstein, and Matthew O’Toole. Wave-based non-line-of-sight imaging using fast f–k migration. *ACM Trans. Graph. (SIGGRAPH)*, 38(4):116, 2019.
- [27] Xiaochun Liu, Sebastian Bauer, and Andreas Velten. Analysis of feature visibility in non-line-of-sight measurements. In *Proc. CVPR*, 2019.
- [28] Xiaochun Liu, Ibon Guillen, Marco La Manna, Ji Hyun Nam, Syed Azer Reza, Toan Huu Le, Adrian Jarabo, Diego Gutierrez, and Andreas Velten. Non-line-of-sight imaging using phasor-field virtual wave optics. *Nature*, 572:620–623, 2019.
- [29] Matthew O’Toole, David B. Lindell, and Gordon Wetzstein. Confocal non-line-of-sight imaging based on the light cone transform. *Nature*, pages 338–341, 2018.
- [30] Matthew O’Toole, David B. Lindell, and Gordon Wetzstein. Real-time non-line-of-sight imaging. In *ACM SIGGRAPH E. Tech.* ACM, 2018.
- [31] R. Pandharkar, A. Velten, A. Bardagjy, E. Lawson, M. Bawendi, and R. Raskar. Estimating motion and size of moving non-line-of-sight objects in cluttered environments. In *Proc. CVPR*, 2011.
- [32] Adithya Kumar Pediredla, Mauro Buttafava, Alberto Tosi, Oliver Cossairt, and Ashok Veeraraghavan. Reconstructing rooms using photon echoes: A plane based model and reconstruction algorithm for looking around the corner. In *Proc. ICCP*, 2017.
- [33] M.J. Prickett and C.C. Chen. Principles of inverse synthetic aperture radar/isar/imaging. In *Proc. EASCON*, 1980.
- [34] Charles Saunders, John Murray-Bruce, and Vivek K. Goyal. Computational periscopy with an ordinary digital camera. *Nature*, 565(7740):472, 2019.
- [35] Sjors H.W. Scheres. Relion: implementation of a Bayesian approach to cryo-EM structure determination. *Journal of Structural Biology*, 180(3):519–530, 2012.

- [36] Dongeek Shin. *Computational imaging with small numbers of photons*. PhD thesis, Massachusetts Institute of Technology, 2016.
- [37] Amit Singer. Mathematics for cryo-electron microscopy. *arXiv preprint arXiv:1803.06714*, 2018.
- [38] Amit Singer and H-T Wu. Two-dimensional tomography from noisy projections taken at unknown random directions. *SIAM J. Imaging Sci.*, 6(1):136–175, 2013.
- [39] Brandon M. Smith, Matthew O’Toole, and Mohit Gupta. Tracking multiple objects outside the line of sight using speckle imaging. In *Proc. CVPR*, 2018.
- [40] Martin Thoma. The hasyv2 dataset. *arXiv preprint arXiv:1701.08380*, 2017.
- [41] C. Thrampoulidis, G. Shulkind, F. Xu, W. T. Freeman, J. H. Shapiro, A. Torralba, F. N. C. Wong, and G. W. Wornell. Exploiting occlusion in non-line-of-sight active imaging. *IEEE Trans. Comput. Imaging*, 4(3), 2018.
- [42] Antonio Torralba and William T. Freeman. Accidental pinhole and pinspeck cameras: Revealing the scene outside the picture. In *Proc. CVPR*, 2012.
- [43] Chia-Yin Tsai, Kiriakos N. Kutulakos, Srinivasa G. Narasimhan, and Aswin C. Sankaranarayanan. The geometry of first-returning photons for non-line-of-sight imaging. In *Proc. CVPR*, 2017.
- [44] Naonori Ueda and Ryohei Nakano. Deterministic annealing em algorithm. *Neural Networks*, 11(2):271–282, 1998.
- [45] A. Velten, T. Willwacher, O. Gupta, A. Veeraraghavan, M.G. Bawendi, and R. Raskar. Recovering three-dimensional shape around a corner using ultrafast time-of-flight imaging. *Nature Communications*, 3:745, 2012.
- [46] A. Velten, D. Wu, A. Jarabo, B. Masia, C. Barsi, C. Joshi, E. Lawson, M. Bawendi, D. Gutierrez, and R. Raskar. Femto-photography: Capturing and visualizing the propagation of light. *ACM Trans. Graph.*, 32, 2013.
- [47] Aparna Viswanath, Prasanna Rangarajan, Duncan MacFarlane, and Marc P Christensen. Indirect imaging using correlography. In *Proc. COSI*, 2018.
- [48] Lingda Wang and Zhizhen Zhao. Two-dimensional tomography from noisy projection tilt series taken at unknown view angles with non-uniform distribution. *arXiv preprint arXiv:1905.10343*, 2019.
- [49] Zhou Wang, Alan C. Bovik, Hamid R. Sheikh, and Eero P. Simoncelli. Image quality assessment: from error visibility to structural similarity. *IEEE Trans. Image Process.*, 13(4):600–612, 2004.
- [50] Di Wu, Gordon Wetzstein, Christopher Barsi, Thomas Willwacher, Qionghai Dai, and Ramesh Raskar. Ultrafast lensless computational imaging through 5d frequency analysis of time-resolved light transport. *Int. J. Comput. Vision*, 110(2):128–140, 2014.
- [51] Shumian Xin, Sotiris Nousias, Kiriakos N. Kutulakos, Aswin C. Sankaranarayanan, Srinivasa G. Narasimhan, and Ioannis Gkioulekas. A theory of fermat paths for non-line-of-sight shape reconstruction. In *Proc. CVPR*, 2019.
- [52] Feihu Xu, Gal Shulkind, Christos Thrampoulidis, Jeffrey H. Shapiro, Antonio Torralba, Franco N. C. Wong, and Gregory W. Wornell. Revealing hidden scenes by photon-efficient occlusion-based opportunistic active imaging. *Opt. Express*, 26(8):9945–9962, 2018.
- [53] Mona Zehni, Shuai Huang, Ivan Dokmanić, and Zhizhen Zhao. Geometric invariants for sparse unknown view tomography. In *Proc. ICASSP*, 2019.